Cross-Domain Spectral Ratio Structure: Refined Recurrence, Robustness and Diagnostic Limits

Jeremy Rodgers

Independent Researcher

Research platform: www.everythingequation.com

Reserved publication DOI: 10.5281/zenodo.23888292

2 November 2026

Abstract

We examine finite structural signatures formed by counting all ordered spectral-value ratios in fifteen fixed relative windows. The constructions are a frozen readout of gravitational Kerr damping rates, a 465-state squared-radial hydrogen coupling-graph Laplacian, and Gaussian graph Laplacians reconstructed from seven previously seen images. Five of six primary image profiles correlate strongly with the hydrogen minimum-normalized log1p profile: at 3% tolerance their fifteen-slot Spearman coefficients range from 0.886 to 0.996. The dark embryo profile is an exception, and Kerr correlations are more moderate. The hydrogen–Kerr coefficient, 0.52143, is essentially preserved by shell-block permutations (mean 0.52137, sample SD 0.00255). Separately, Kerr exceeds all 4,999 conditional uniform-group references in both development and angular holdout; only 10 and 22 phase-bin references reach its scores. An overtone-trend/Gram-preserving reference is more permissive on holdout. Hydrogen abundance is readout-dependent: raw UNION incidence exceeds all 99 shell controls, whereas the primary transformed incidence does not. A short fiber pilot moves too little to inform the target statistic. The paired alternative-library joint fraction is 0.2339, failing the frozen criterion of at most 0.05; profile recurrence therefore does not establish exclusive privilege of the original library. We derive the exact log-spectrum autocorrelation representation, with multiplicities, self-pair removal and native cutoffs, and distinguish this identity from independent density prediction. Consecutive-gap ratios and covariance universality provide complementary theoretical tools, but neither has been demonstrated to explain these operators quantitatively. The supported result is a reproducible finite structural signature and a diagnostic method for comparing these constructions, with control-specific discrimination and precisely delimited robustness.

Keywords: spectral-value ratios; graph Laplacians; Kerr quasinormal modes; conditional controls; structural recurrence; reproducibility.

The DOI above is reserved for this manuscript. No public deposition is asserted by this prepublication version.

© 2026 Jeremy Rodgers. New text, figures and tables: CC BY 4.0.

1 Research question and contributions

Different spectral constructions can produce similar distributions of dimensionless ratios. Such recurrence can be scientifically useful without uniquely identifying a physical system or privileging a named set of constants. Its interpretation depends on the operator, readout, selected modes, counting convention and information preserved by the comparison model. We ask which finite profile similarities recur across the specified constructions, which perturbations preserve them, and which conditional references discriminate the observed incidence.

The measurement scheme uses fifteen fixed centers, including familiar irrational constants and rational fractions. We call the measured finite vector a *structural signature*: an operational descriptor of this construction and readout. The term does not imply a general-purpose classifier, an inverse reconstruction of geometry, or a universally identifying physical fingerprint. Library specificity is a separate empirical question, tested against the same retained alternative libraries in all domains.

Three findings motivate the analysis. First, the primary hydrogen profile and five reconstructed image profiles have strong descriptive shape agreement, with a persistent embryo exception. Second, specified Kerr conditional references give substantial discrimination, while shell-preserving hydrogen perturbations leave much of the cross-domain shape intact. Third, the original library fails the frozen joint specificity criterion. These observations are compatible: recurrence, robustness and exclusive library advantage are different properties.

The contributions are (i) explicit native constructions and complete paired profile comparisons; (ii) a preservation-aware account of conditional discrimination and robustness, including unsuccessful comparisons; and (iii) an exact mathematical representation connecting spectral-value ratios to log-spectrum autocorrelation. We integrate consecutive-gap statistics [1] and correlated covariance modelling [2] to identify the explanatory tests still required. No additional density-model or gap-statistics experiment is reported as completed evidence.

2 Inputs, operators and provenance

2.1 Gravitational Kerr damping spectra

The development input contains 540 labelled gravitational modes with spin weight $s = -2$, angular orders $\ell = 2, \ldots, 6$, every $m = -\ell, \ldots, \ell$, physical overtones $n = 0, 1, 2, 3$, and dimensionless spins $a/M = 0, 0.5, 0.9$. The positive rate is

$$\begin{aligned} \lambda_j &= -2\,\mathrm{Im}(M\omega_j), \qquad D_K = \mathrm{diag}(\lambda_j), \\ v_j &= f_T(\lambda_j) = \frac{1 - e^{-T\lambda_j}}{T\lambda_j}, \qquad T = 12.115276586285876. \end{aligned} \tag{1}$$

The archived rate units and this readout are retained without a new mean or range normalization. Numerical evaluation uses $-\mathrm{expm1}(-T\lambda)/(T\lambda)$. The modes originate in the Kerr catalogue associated with Berti et al. [3]; the independently acquired angular holdout uses the `qnm` implementation [4].

The earlier prospective holdout contains 684 labelled modes, replacing the angular orders by $\ell = 8, 9, 10$ while retaining the same overtones and spins. Its acquisition followed the specificity freeze. It tests angular-family generalization, not a new spin range. There are 228 related mode families; the maximum root residual was 2.81×10^{-12}. Exact Schwarzschild m-degeneracies at zero spin are retained. Neither 540 nor 684 is a count of independent black-hole observations. The subsequent cross-domain experiment uses the development spectrum and existing library bank; it does not create another Kerr holdout.

The historical approximately 12.3 standardized effect and 2.33 readout-width pair belongs to an electromagnetic run, not this gravitational selection. Our principal Kerr evidence is the reproduced count and the specified 4,999-reference comparisons below. Section E records the material numerical corrections.

2.2 The 465-state hydrogen coupling graph

Vertices are (n, ℓ) with $1 \le n \le 30$, $0 \le \ell < n$, giving 465 states. For $|\ell - k| = 1$, the symmetric edge weight is the squared radial dipole integral in atomic units,

$$W_{(n,\ell),(m,k)} = \left| \int_0^\infty R_{n\ell}(r)\, r\, R_{mk}(r)\, r^2\, dr \right|^2, \qquad L_H = D - W, \quad D_{ii} = \sum_j W_{ij}, \quad W_{ii} = 0. \tag{2}$$

There are 8,990 undirected allowed edges, including 435 same-n edges. The retained exact rational squared weights and state order define the numerical graph. Angular factors and an expanded magnetic-state basis are not inserted. The 464 positive eigenvalues supply the primary readout

$$v_i = \log\left(1 + \frac{\lambda_i}{\lambda_{\min,+}}\right), \tag{3}$$

with raw positive eigenvalues a named secondary view. This is a coupling-graph Laplacian, not the physical hydrogen energy Hamiltonian. Accordingly, a statistic of these modes cannot automatically be interpreted as atomic energy-level chaos or integrability.

The native construction was checked using exact same-n identities, independent radial fixtures, a separate eigenspectrum calculation, and full eigenpair residuals. The relative eigenpair residual was approximately 1.16×10^{-15}. These checks validate the stated finite operator; they do not recover an unavailable historical run with different reported totals.

2.3 Previously seen image reconstructions

For each supplied image, threshold-component centroids define a point cloud. The complete Gaussian graph and its combinatorial Laplacian are

$$W_{ij} = \exp\left[-\frac{\|x_i - x_j\|^2}{2\sigma_d^2}\right] \ (i \ne j), \quad W_{ii} = 0, \quad \sigma_d = \mathrm{median}_{i<j}\, \|x_i - x_j\|, \quad L_I = D - W. \tag{4}$$

Positive modes are divided by their mean before counting. This common scalar cancels in all value ratios. The operator is the weighted combinatorial Laplacian, not a normalized graph Laplacian or an image Fourier transform [5].

Preprocessing applies EXIF orientation, resizes the longest side to at most 512 pixels using Lanczos without upsampling, composites transparency onto white, and computes luminance with stored-sRGB weights $(0.2126, 0.7152, 0.0722)$. Dark masks use strict thresholds $g < 0.25, 0.5, 0.75$; bright sensitivities use $g > 0.25, 0.5, 0.75$. Eight-connected components of inclusive area 4–2,500 pixels yield unweighted pixel-center centroids. Threshold and component scan order are retained; a candidate is kept only if its distance from every earlier retained centroid exceeds two pixels. There is no feature truncation, crop, contrast adjustment or post-score retuning. Fewer than three retained points or more than 2,000 nodes triggers a fixed failure/resource gate, rather than truncating the input. Appendix A specifies zero-mode handling.

The six dark primary source families are embryo, galaxy, pollen-like microscopy, leaf, Shroud and snowflake. The adult stock portrait is exploratory. All seven bright versions are dependent sensitivity views, not additional independent objects. Table 1 gives the retained counts. All 14 variants passed independent extraction, eigenpair and bounded counter checks; the maximum relative eigenpair residual was 1.39×10^{-15}.

Table 1: Retained image reconstructions. Primary family labels identify the supplied subjects, not independently validated biological or physical landmarks. All inputs were previously seen. The portrait is exploratory; bright variants are secondary.

Source	Dark points	Bright points	Dark modes	Dark N_R
Embryo	31	36	30	870
Galaxy	111	307	110	11,990
Pollen-like microscopy	1,000	1,134	999	997,002
Leaf	572	383	571	325,470
Shroud	393	287	392	153,272
Snowflake	704	631	703	493,506
Adult portrait (exploratory)	53	71	52	2,652

These are new, documented reconstructions of the main Gaussian-Laplacian method, not exact replications of the earlier image table or unseen holdouts. Components include backgrounds, membrane boundaries, stars, watermarks and cloth damage. The pollen-like file has an exact byte match to Dartmouth's microscopy gallery; six exact acquisition mappings and all seven photographic redistribution permission records remain unresolved. The public supplement supplies numerical coordinates, source hashes and the extraction specification, but does not redistribute the photographs. Graph-level numerical regeneration is consequently distinct from fully independent pixel-level acquisition and replay. No authenticity, formation, age or intentional-encoding conclusion is drawn from any image profile.

3 Ratio statistics and mathematical foundations

3.1 Finite window profiles

For a positive readout multiset $v = (v_1, \dots, v_n)$, let $\mathcal{E}$ contain the ordered pairs (i, j), $i \neq j$, meeting the native ratio filter, and let $N_R = |\mathcal{E}|$. Kerr uses $0.05 < v_i/v_j < 5$; hydrogen and spatial readouts have no finite upper cut. The retained centers in their fixed slot order are

$$\begin{aligned}(c_1, \dots, c_{15}) = (&\varphi, \varphi^{-1}, \varphi^2, \sqrt{2}, \sqrt{3}, \sqrt{5}, \pi, \pi/2, \pi/10,\\ &e, e^{-1}, \ln 2, j_{0,1}, 3/13, 1/7),\end{aligned} \tag{5}$$

where $j_{0,1}$ is the first positive zero of J_0. The fine-structure constant is not a member of this fifteen-slot scheme. At relative tolerance ϵ,

$$h_j = \sum_{(a,b)\in\mathcal{E}} \mathbf{1}\{c_j(1-\epsilon) \le v_a/v_b \le c_j(1+\epsilon)\}, \qquad p_j = h_j/N_R. \tag{6}$$

$$\begin{aligned}A_{\mathrm{SUM}} &= \frac{\sum_j h_j}{N_R},\\ A_{\mathrm{UNION}} &= \frac{1}{N_R} \sum_{(a,b)\in\mathcal{E}} \mathbf{1}\{v_a/v_b \in \bigcup_j [c_j(1-\epsilon), c_j(1+\epsilon)]\}.\end{aligned} \tag{7}$$

SUM counts overlap multiplicity; UNION counts a ratio once. The structural signature is the native incidence vector $p = (p_1, \dots, p_{15})$. It is not a vector of null-relative enrichments. Reciprocal and power-related centers, shared ratios and overlapping windows induce dependence; fifteen slots do not provide fifteen independent physical observations.

All analyses retain $\epsilon = 0.03, 0.01, 0.005$. Native primary abundance uses Kerr 3% SUM, hydrogen minimum-normalized log1p 3% UNION and spatial 1% UNION. Profile correlations compare domains at the *same* tolerance, at all three widths. Spearman correlation with average

ranks for ties is primary descriptive; Pearson is secondary. No iid-slot significance test is used. Multiplying one nonzero profile by a positive scalar does not change either correlation, so h/N_R and h/SUM have the same within-profile shape correlation while retaining different abundance interpretations.

3.2 Exact log-autocorrelation representation

Set $u_i = \log v_i$, $\mu_n = n^{-1}\sum_i \delta_{u_i}$, and let $\check{\mu}_n$ be reflection about zero. The unfiltered, normalized nonself log-ratio measure is

$$\nu_n = \frac{1}{n(n-1)}\sum_{i\neq j}\delta_{u_i-u_j} = \frac{n}{n-1}\mu_n * \check{\mu}_n - \frac{1}{n-1}\delta_0. \tag{8}$$

Indeed, the convolution contains all n^2 ordered terms; exactly n are diagonal self-pairs. Distinct equal-valued modes still contribute at zero after subtraction. Multiplicities must therefore be retained rather than deduplicated.

A matching window becomes

$$I_j = [\log c_j + \log(1-\epsilon),\ \log c_j + \log(1+\epsilon)]. \tag{9}$$

Writing $B = \mathbb{R}$ for the uncut positive-ratio cases and $B = (\log 0.05, \log 5)$ for Kerr gives the exact native statistic

$$p_j = \frac{\nu_n(I_j \cap B)}{\nu_n(B)}, \qquad N_R = n(n-1)\nu_n(B). \tag{10}$$

Closed matching windows and open native cutoffs remain distinct. SUM adds these masses with multiplicity; UNION measures the union of the windows. Relative windows are not exactly symmetric in log coordinates. Complete ordered pairs force symmetry of ν_n, but Kerr's asymmetric conditioning interval need not preserve reciprocal balance of the conditioned distribution.

The relevant log-spectrum is $\log v$: for primary hydrogen it is $\log\log(1+\lambda/\lambda_{\min,+})$, not simply $\log\lambda$. Spatial mean normalization only translates the log-spectrum. With Fourier convention $\widehat{\eta}(k) = \int e^{ikt}\eta(dt)$, the unnormalized nonself difference measure obeys

$$n(n-1)\widehat{\nu}_n(k) = \left|\sum_i e^{iku_i}\right|^2 - n. \tag{11}$$

This is a log-native-coordinate form-factor identity. It is not an already unfolded, ensemble-averaged GOE form factor. Equations (8)–(11) exactly characterize the measurement; replaying a profile from its own complete spectrum is not an independent explanation.

4 Frozen comparison design and control definitions

4.1 Paired alternative libraries

The same target and 9,999 retained G libraries, with original identities and slot order, are used in all domains. G is a development-informed, Kerr-designed reference population, not a universal distribution over constant libraries. It moves thirteen centers conditional on two fixed endpoints and mechanical geometry constraints: slot cells and ordering, below/above-one counts, relative widths, summed and union *linear* window coverage at all three tolerances, and the two individual 3% overlaps. Individual log-window widths and summed log coverage are common; 3% log-union coverage is only approximately matched. The logarithmic union range is 0.846268–0.848952, versus target 0.847440. No library is rejected because it scores well in a new domain.

For each observed native dataset d, let $s_d(b)$ be its primary abundance for library b and define the symmetric midposition over all $M = 10,000$ identities by

$$P_d(b) = \frac{\#\{a : s_d(a) < s_d(b)\} + \frac{1}{2}\#\{a : s_d(a) = s_d(b)\}}{M}. \tag{12}$$

Spatial positions are averaged equally within each source family and then equally over the six primary families; this aggregate is reranked by the same midposition rule to obtain P_I. Here each primary family contributes its one dark version. The joint statistic and frozen reference fraction are

$$Q(b) = \min\{P_K(b), P_H(b), P_I(b)\}, \qquad F_Q = \frac{\#\{b : Q(b) \geq Q(\text{target})\}}{M}. \tag{13}$$

The specified criterion is $F_Q \leq 0.05$, including target and ties. It is a conditional saved-population comparison, not the probability that the research is false, the fraction of data explained, or proof that alternative libraries are equivalent coordinate projections.

The earlier Kerr specificity prediction is distinct: both development and the then-new angular holdout had to give one-sided 95% upper bounds at most 0.05 for the G exceedance probability. The secondary S bank additionally retains specified algebraic families with four fixed anchors; it cannot replace a failed primary G conjunction. All images and the later reused Kerr data are previously seen.

4.2 Kerr U, R and P references

Each dataset/reference combination contains 4,999 eligible spectra at the frozen point. These are specified statistical references, not new numerical solutions of the Kerr equations.

U: conditional uniform transformed groups.
Exact zero-spin m-copies sharing (ℓ, n, a) form a group; other modes are singleton groups. There are 380 unique centers in development and 468 in holdout. U holds fixed the observed minimum and maximum *Fejér-readout* values and their group identities, draws the other centers independently uniformly on that transformed interval, and restores each fixed multiplicity. It preserves the endpoints and physical degeneracies, while changing transformed density, overtone ordering and spin/mode correlations. It is not uniform sampling of raw damping rates followed by the readout.

R: raw-rate overtone residual orbit.
For every fixed (ℓ, m, a), fit the four *linear raw rates* λ_n, $n = 0, \ldots, 3$, by ordinary least squares on $(1, n)$. A common Haar $O(2)$ action, independently drawn for each ℓ, rotates or reflects the two-dimensional residual complement for every m and spin in that block. Re-add the raw-rate fits and apply Eq. (1). R preserves each intercept, slope, row mean and sum of squares, and the full within-ℓ residual Gram matrix. It changes residual orientation in overtone coordinates and cross-ℓ relationships; it does not preserve every fixed-n distribution or the complete empirical density.

P: common phase within labelled raw-log bins.
Write $\log \lambda_i / 0.25 = b_i + f_i$, with b_i integer and $0 \leq f_i < 1$. For each ℓ, draw one uniform $\theta_\ell \in [0, 1)$, replace the raw log rate by $0.25[b_i + (f_i + \theta_\ell \bmod 1)]$, exponentiate and apply the frozen readout. P preserves every labelled bin index, hence all corresponding coarse histograms, within-block circular phase differences and exact degeneracies. It changes fine within-bin placement and the complete empirical distribution.

R and P impose the frozen positivity and overtone-order eligibility checks. All 29,994 proposals across the two datasets and three references were eligible; no score-based rejection occurred. The laws preserve different information and are not a nested hierarchy. For observed incidence A, report $k = \#\{A_b \geq A\}$ and the add-one reference fraction $(k+1)/(B+1)$. Monte Carlo intervals,

where used, describe numerical integration error under the specified law, not uncertainty from independent physical catalogue observations. A physical randomization interpretation additionally needs the corresponding group/model symmetry; it is not derived from the word "noise."

4.3 Hydrogen shell and finite-fiber pilots

The shell reference independently permutes the weights within each unordered principal-shell pair $\{n, m\}$, including same-shell blocks. It preserves the allowed support and the *entire weight multiset* in each block, including detailed radial information; placement at ℓ-labelled edges changes and vertex strengths generally do not remain fixed. There are 99 retained endpoints.

The second pilot starts separately from the observed nonnegative edge vector at every endpoint and takes 64 specified fiber steps. Its linear constraints retain vertex strengths, shell-pair totals, and edge-weighted crossmoments with fixed covariates

$$g_1 = |n - m|(\ell + k + 1), \qquad g_2 = nm(\ell + k + 1)^2. \tag{14}$$

It is nonnested with shell permutations, since it need not retain block multisets. Its 99 finite-step endpoints are diagnostic, not certified equilibrium or mixed samples. No automatic extension of the pilot was performed.

For either pilot, a reported standardized difference is $\Delta/s = (A_{\text{obs}} - \bar{A})/s$, using the sample SD with denominator 98. It is a descriptive effect, not an extreme-tail Gaussian probability. The retained target, both readouts, all three tolerances and all endpoints are used without favorable redraws.

5 Cross-domain profile recurrence

5.1 Observed shapes and the embryo exception

The observed comparison has 17 views: Kerr, two hydrogen readouts and 14 spatial variants. The primary descriptive core contains Kerr, hydrogen log1p and the six dark families. All original library identities, all fifteen slots and all three tolerances are retained. Figure 1 and Appendix D show every core-domain pair, including image–image comparisons; the supplement supplies the full 17-view results.

Table 2: Primary hydrogen log1p versus the six dark image signatures. $F_{G,s}$ is the fraction of all 10,000 paired library coefficients at least the target coefficient, including target and ties; it is descriptive.

	Spearman at tolerance			Pearson	$F_{G,s}$
Source	3%	1%	0.5%	3%	3%
Embryo	0.23900	0.26856	0.04482	-0.25984	0.54060
Galaxy	0.92063	0.92328	0.96373	0.98928	0.97900
Pollen-like	0.88641	0.88641	0.88518	0.95464	0.86000
Leaf	0.99553	0.99463	0.99642	0.98673	0.16900
Shroud	0.94868	0.94492	0.94765	0.97981	0.71350
Snowflake	0.98743	0.98652	0.98921	0.99637	0.44180

At 3%, five hydrogen–image Spearman coefficients lie between 0.886 and 0.996 (Table 2); they remain 0.885–0.996 at the two narrower widths. This is a substantial recurring shape in the declared constructions. Embryo dark is a clear exception: its coefficients are 0.239, 0.269 and 0.045, and its Pearson coefficients are negative at all three widths. Its bright version differs strongly, but is retained as a sensitivity rather than promoted after seeing the primary result. The image–image coefficients among the other five primary families are also high; their 3%

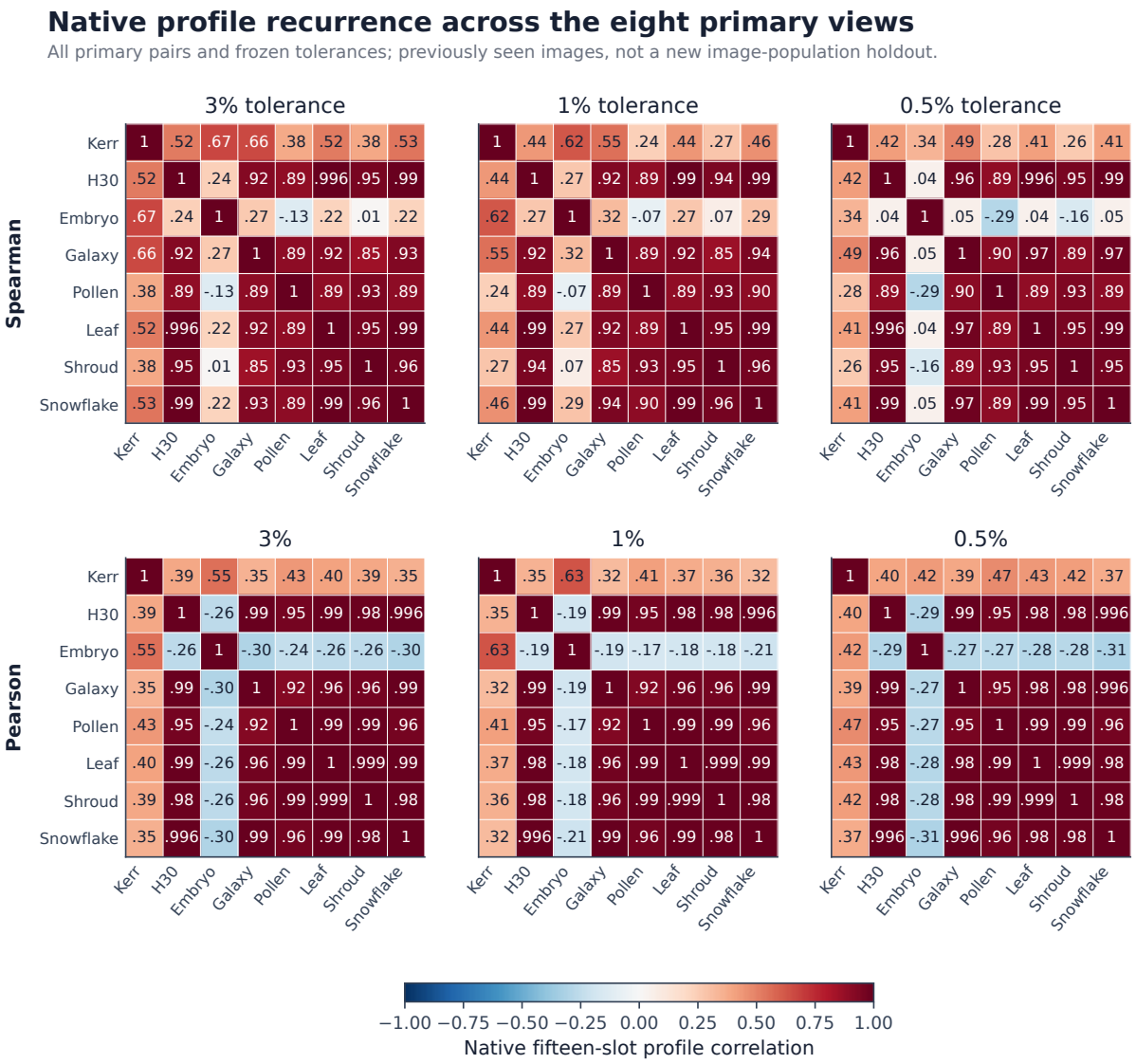


Figure 1: Complete primary-core profile comparisons at all three tolerances. Spearman is primary descriptive and Pearson secondary. Each coefficient uses the fifteen retained incidence slots, with ties and algebraic dependence retained. These are value-ratio profile correlations, not adjacent-gap statistics, null-excess correlations or repetitions of earlier full-histogram correlations.

Spearman range is 0.851–0.988. The pattern is consequently broad but heterogeneous, not a universal image profile.

Kerr's relationship to the other domains is more moderate. At 3%, its Spearman coefficients are 0.52143 with hydrogen, 0.66848 with embryo, 0.65708 with galaxy, 0.38277 with pollen-like microscopy, 0.52189 with leaf, 0.38399 with Shroud and 0.53335 with snowflake. These pairs and their narrower-width outcomes remain visible rather than being summarized solely by the five high hydrogen–image values.

5.2 Alternative-library profile comparisons

High target coefficients frequently have high counterparts under the same paired G libraries (Figure 2). For hydrogen versus the six dark families, the 36 coefficient/tolerance descriptions have conservative fractions at least the target ranging from 0.0598 to 0.9790. Thus the high native resemblance is not itself evidence of exceptional target-library similarity in this population.

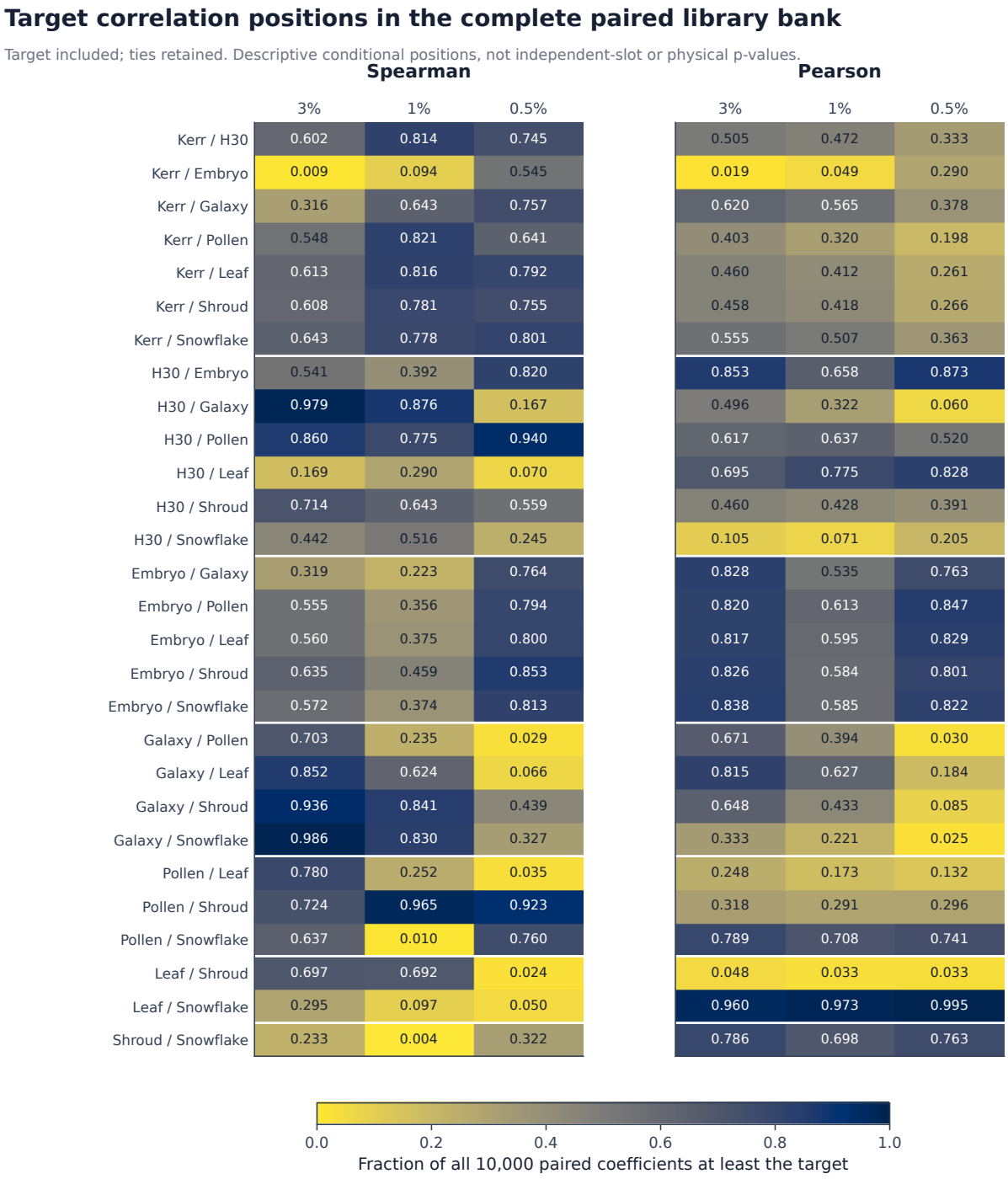


Figure 2: Positions of every primary-core target correlation in the complete paired alternative-library population. Fractions include target and ties. They describe target specificity relative to this retained bank, not physical discovery probabilities or independently sampled image replications. All 28 unique pairs, three widths and both coefficients are retained.

There are source- and width-specific exceptions to that general pattern. Kerr–embryo at 3% gives Spearman 0.66848 and fraction 0.0086 (Pearson 0.54929, fraction 0.0190), weakening at narrower widths. This is a descriptive result among many retained pairs, not a substitute primary test. Both conservative fractions and symmetric midpositions are supplied because exact coefficient ties can be substantial. No new selected significance threshold is imposed on this matrix of comparisons.

6 Conditional discrimination and profile robustness

6.1 Kerr conditional-control successes and their boundary

The observed development and angular-holdout incidences are

$$A_3^{\mathrm{dev}} = \frac{83,194}{272,049} = 0.3058052, \qquad A_3^{\mathrm{hold}} = \frac{138,984}{436,928} = 0.3180936.$$

Under U, none of 4,999 controls reaches either observed incidence. Under P, only 10 development and 22 holdout controls do so (Table 3). These results establish substantial discrimination against the specified transformed-uniform group model and the coarse-bin/phase-orbit model. P's effect is especially informative because every labelled coarse raw-log bin and within-block circular difference is retained.

Table 3: Kerr conditional comparisons at the frozen 3% SUM point. Each row has $B = 4,999$. ΔA is observed minus reference mean. Add-one fractions are conditional-reference summaries, not probabilities of a physical hypothesis being false.

Data	Reference	k	$(k+1)/5000$	Mean incidence	ΔA
Development	U	0	0.0002	0.24540	0.06041
Holdout	U	0	0.0002	0.24468	0.07341
Development	P	10	0.0022	0.26680	0.03901
Holdout	P	22	0.0046	0.26506	0.05304
Development	R	20	0.0042	0.28062	0.02518
Holdout	R	757	0.1516	0.31049	0.00760

R provides consequential counterevidence: 757 of 4,999 holdout controls reach the observed score, versus 20 in development. Strong holdout discrimination beyond the retained raw overtone trends and residual Gram structure is therefore not demonstrated. The contrast with U and P preserves the positive conditional findings while restricting their interpretation. Since the laws are nonnested, it is not a proof that one uniquely identified layer of physical information causes the incidence. It is also not evidence that all domains defeat every noise or artifact explanation.

6.2 Shell-block preservation of hydrogen cross-domain shape

Shell permutation changes weight placement substantially: the relative edge-vector displacement is approximately 0.562–0.648. Nevertheless, the primary hydrogen–Kerr Spearman coefficient changes from 0.521429 to a shell mean 0.521370, SD 0.002551. Its observed-minus-mean difference is only 0.02297 sample SD. The six primary hydrogen–image coefficients are similarly close to their shell means (Table 4; Figure 3).

Table 4: Primary hydrogen log1p, 3%: native cross-domain Spearman coefficients and the 99 shell-permutation replacements. Other domains are held observed. The standardized differences are descriptive; SD is endpoint variability, not a confidence interval for independent physical sources.

Other view	Observed	Shell mean	Sample SD	$(\rho - \bar{\rho})/s$
Kerr	0.52143	0.52137	0.00255	0.02297
Embryo	0.23900	0.23732	0.00506	0.33137
Galaxy	0.92063	0.92081	0.00040	-0.45749
Pollen-like	0.88641	0.88634	0.00094	0.07218
Leaf	0.99553	0.99479	0.00196	0.37787
Shroud	0.94868	0.94864	0.00090	0.04428
Snowflake	0.98743	0.98848	0.00169	-0.62409

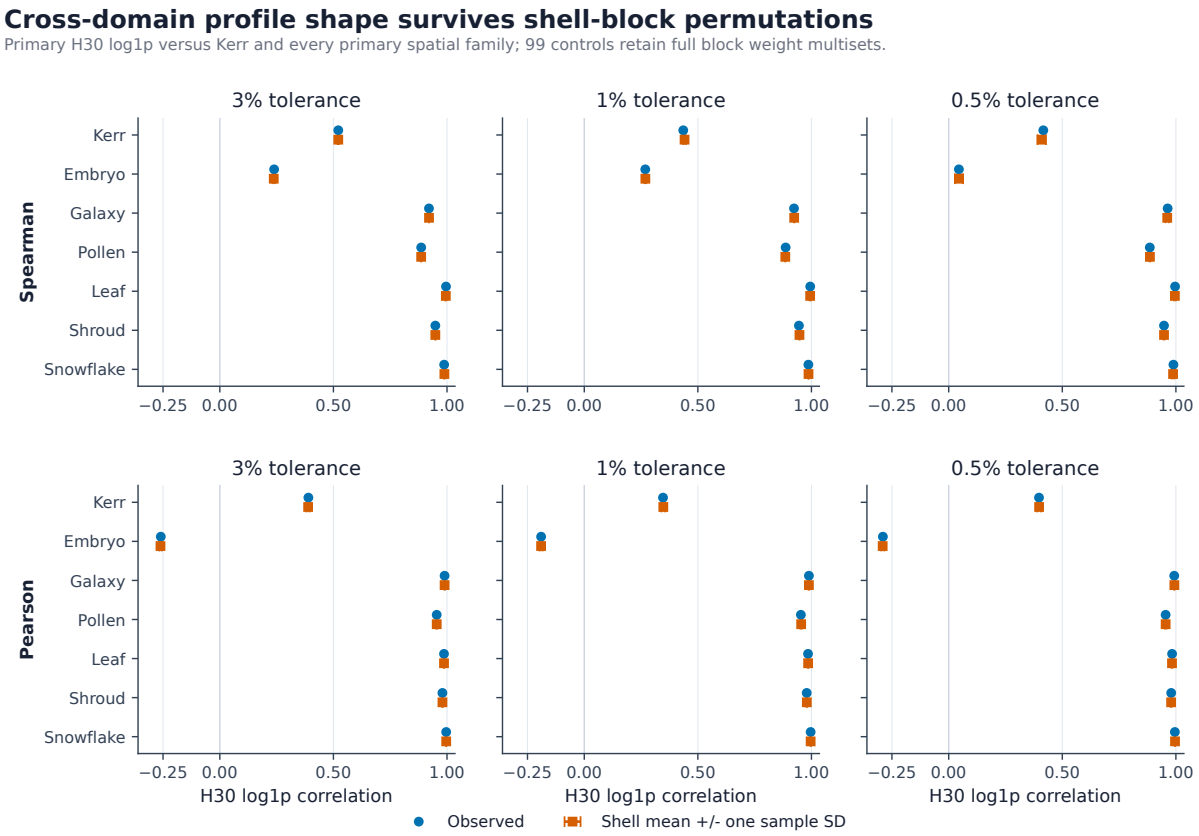


Figure 3: Shell-block robustness of native profile shape. Observed primary hydrogen–Kerr and hydrogen–six-dark-image coefficients are compared with the means and sample SDs of all 99 shell replacements at every width, for both Spearman and Pearson. The other view in each pair is held observed. Persistence is conditional on retained block multisets and does not certify spectral rigidity or joint null-excess recurrence. The complete raw secondary and sensitivity-view comparisons are supplied electronically.

This is profile robustness under a perturbation that retains detailed shell-block weight multisets. It does not establish random-matrix *spectral rigidity*, which would require an appropriate statistic or theorem. Nor does it show that all quantum/radial structure has been removed. At 3%, the cross-domain Spearman differences range from -0.624 to $+0.378$ sample SD; the Pearson differences range from -0.347 to $+0.254$. The complete raw/log, width, coefficient and sensitivity-view summaries are retained in the supplement; Figure 3 displays every primary cross-domain anchor for the hydrogen log1p readout at all widths with both coefficients. Raw secondary profile results are also supplied, rather than inferred from the transformed view.

These conditional replacements vary only one hydrogen view while holding Kerr, the images and the other hydrogen view observed. They do not simulate joint cross-domain uncertainty. Native h/N_R correlation must also be distinguished from correlation of $p - \mathbb{E}_0 p$ or standardized null excess. Paired per-library/per-slot Kerr and spatial null moments are not available in this experiment. Hydrogen's own null moments cannot be broadcast to manufacture cross-domain null-excess correlations. This availability boundary does not erase the separate inherited Kerr reference results.

6.3 Hydrogen abundance and the uninformative fiber pilot

The raw 3% UNION incidence is $26,122/214,832 = 0.1215927$. The shell mean is 0.1203374, SD 0.00043448; none of 99 controls reaches the observation, giving descriptive $\Delta/s = +2.88916$. The

primary transformed incidence is $21,892/214,832 = 0.1019029$, below its shell mean 0.1032113, SD 0.00085315, with $\Delta/s = -1.53358$ and 92 of 99 controls reaching it. SUM has the same readout-dependent signs (Table 5). Raw abundance discrimination and transformed profile robustness are therefore different findings; neither should replace the other.

Table 5: Hydrogen shell controls at 3%. Incidences use all 214,832 ordered nonself pairs. Raw is secondary and log1p primary. Standardized differences are finite-pilot descriptions, not calibrated extreme-tail probabilities.

Readout	Count	Observed	Shell mean	Sample SD	Δ/s	$k/99$
log1p	UNION	0.101903	0.103211	0.000853	-1.53358	92/99
Raw	UNION	0.121593	0.120337	0.000434	2.88916	0/99
log1p	SUM	0.109365	0.110799	0.000965	-1.48664	91/99
Raw	SUM	0.129650	0.128180	0.000496	2.96446	0/99

The fiber endpoints move only 5.78×10^{-10} to 1.23×10^{-9} relative to the parent weight vector. Although all 99 spectra are numerically distinct at the specified tolerance, all 90 target slot/readout/width incidences are unchanged. Both target aggregate statistics and all 204 target conditional coefficient summaries have zero sample variance. The actual-statistic informativeness gate fails: standardized effects are undefined, not evidence of strong significance. A 64-step restart can preserve unprescribed fine structure through locality; this pilot cannot show that its named constraints alone suffice or that the fiber has mixed.

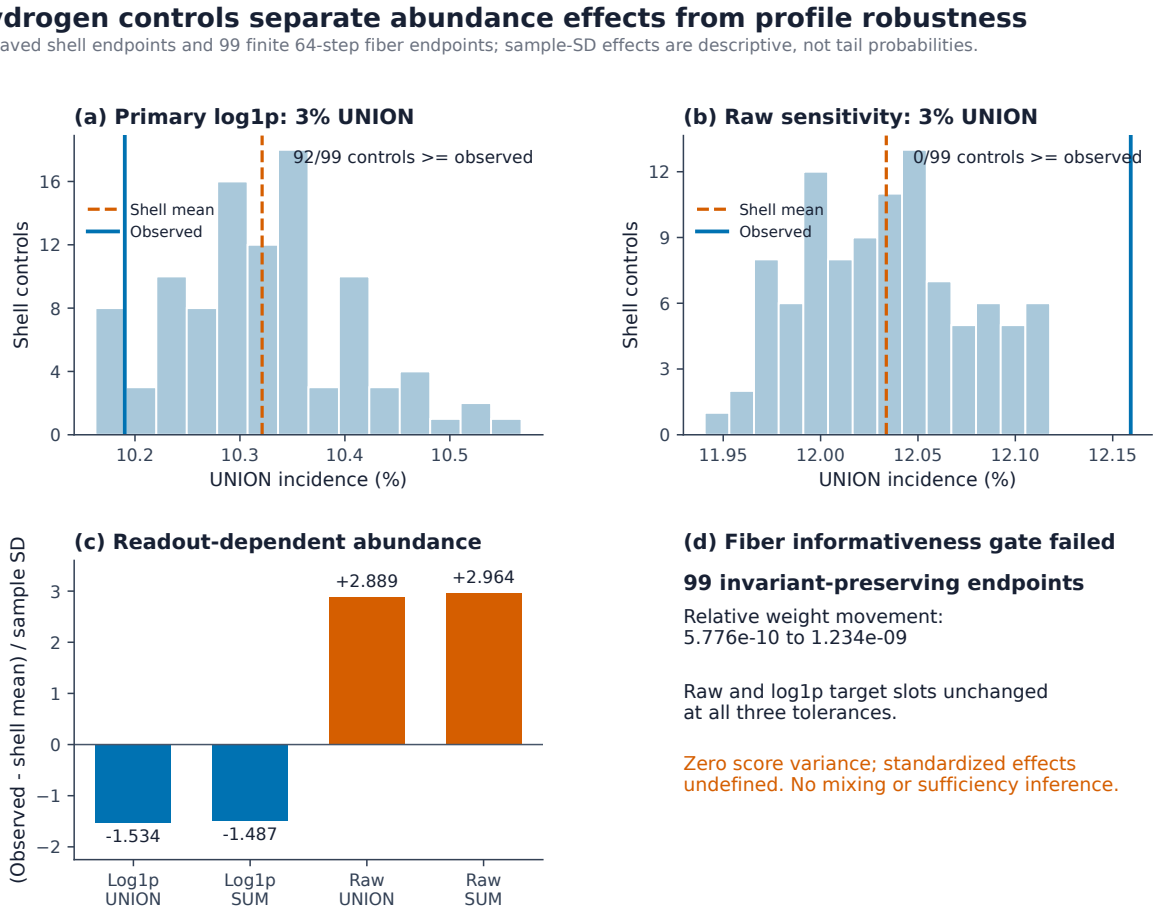


Figure 4: Hydrogen abundance under the retained controls. Panels (a,b) show all 99 UNION outcomes separately for the transformed and raw readouts; panel (c) compares their UNION and SUM standardized differences. Raw and transformed observations lie on different sides of their reference means. Panel (d) shows the fiber pilot's negligible weight motion and zero target score variance. No normal-tail extrapolation is made from these finite pilots.

7 Alternative-library specificity and diagnostic boundaries

The target's joint components are $P_K = 0.95435$, $P_H = 0.44780$ and $P_I = 0.56665$, giving $Q = 0.44780$. Exactly 23.39% of the retained target-plus-G population reaches or exceeds that joint statistic. The frozen $F_Q \leq 0.05$ criterion therefore fails (Figure 5). This result does not establish that the original fifteen centers have an unusual simultaneous advantage across all three native domains.

The earlier Kerr G ranks were 457/10,000 in development and 953/10,000 on angular holdout. Their add-one fractions were 0.0457 and 0.0953; one-sided 95% upper bounds were approximately 0.04919 and 0.10018. The frozen conjunction fails on holdout. The target nevertheless exceeds the G mean in each dataset by 0.03141 and 0.03323 incidence units. A higher absolute holdout incidence does not rescue a failed rank prediction. The secondary S ranks, 135 and 743, also do not give top-5% holdout performance.

These specificity results qualify a library advantage, not the existence of the measured recurrence or the U/P discrimination. Conversely, strong profile correlations and favorable conditional controls do not convert the failed specificity prediction into confirmation of an untested universal replacement. G was mechanically matched in Kerr; its density-weighted effects under another native operator are empirical comparisons, not a demonstrated mathematical coordinate mapping.

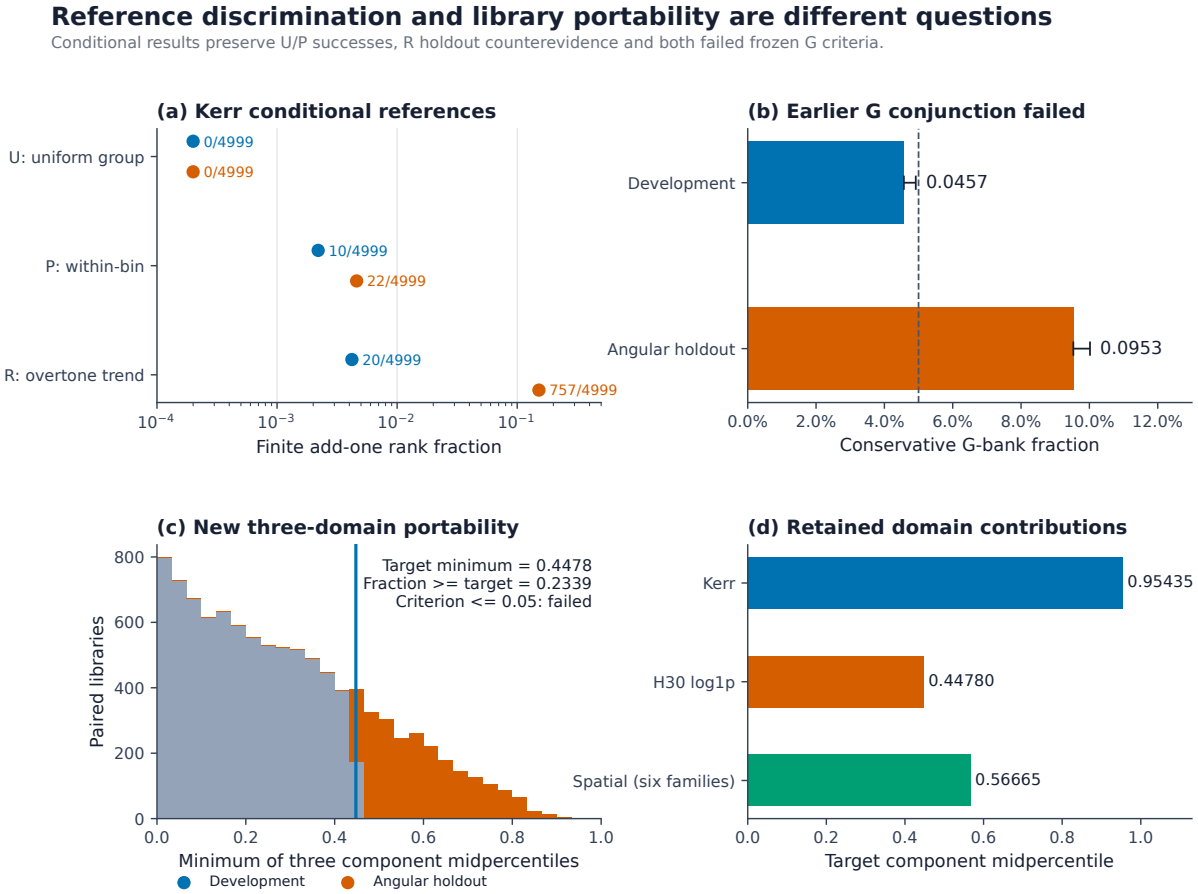


Figure 5: Distinct inferential questions remain distinct. (a) Kerr U/P/R conditional-reference comparisons. (b) Earlier G-library specificity: bars are add-one rank fractions and right caps are one-sided 95% Clopper–Pearson upper bounds; both bounds had to lie below the dashed 5% line. (c,d) The subsequent cross-domain paired-G minimum and target component midpositions use the development Kerr anchor and six previously seen image families. Positive conditional-control discrimination and failed frozen library criteria are both retained.

8 Local spectral statistics and covariance universality

8.1 Consecutive gaps are a complementary observable

For ordered levels $E_1 < \cdots < E_n$, Atas et al. [1] study gaps $s_i = E_{i+1} - E_i$, consecutive ratios $r_i = s_i/s_{i-1}$, and folded ratios $\tilde{r}_i = \min(r_i, r_i^{-1})$. A gap ratio uses three adjacent levels. On 464 distinct levels it yields 462 overlapping observations, not the 214,832 ordered value ratios used here. Gap ratios are exactly invariant under positive affine changes $E \mapsto aE + b$; all-pair value ratios are scale-invariant but generally not shift-invariant.

The cancellation of a common local spacing scale makes gap ratios useful without explicit spectral unfolding. Arbitrary nonlinear readouts are not exactly invisible: cancellation is local when the density or transformation varies slowly across neighboring gaps. Symmetry sectors, unresolved degeneracies, edges and finite size need separate handling. The Ising application in Atas et al. [1] explicitly resolves translation sectors; real symmetry of an arbitrary structured graph does not by itself establish GOE statistics.

Their Gaussian-ensemble three-level surmise is

$$P_\beta(r) = \frac{(r + r^2)^\beta}{Z_\beta (1 + r + r^2)^{1+3\beta/2}}, \qquad \beta = 1, 2, 4, \tag{15}$$

while a stationary Poisson level process gives $P(r) = (1+r)^{-2}$. These are laws for *gap* ratios. The GOE folded-mean surmise $4-2\sqrt{3} \simeq 0.53590$ differs from their large-matrix numerical mean near 0.5307. The paper derives an exact limiting GUE comparison using the sine-kernel process and documents finite-size corrections. Neither that limiting result nor Eq. (15) predicts arbitrary all-pair value-ratio window masses. No gap-statistics experiment on the present constructions has been executed.

8.2 Global density is distinct from local universality

Levi and Oz [2] study feature-feature sample covariance matrices $\Sigma_M = XX^T/M$, where columns of $X \in \mathbb{R}^{d\times M}$ are centered/normalized samples. Their natural-image datasets have a bulk rank relationship $\lambda_i \propto i^{-1-\alpha}$, separated from leading outliers and small-eigenvalue tails. A correlated Gaussian model uses a positive diagonal population covariance formed from the singular values of a Toeplitz construction $T_{ij} = I_{ij} + c|i-j|^{\alpha}$; its sample covariance is Wishart. Generalized Marchenko–Pastur theory provides a density model conditional on that population and the aspect ratio d/M.

The distinction between broad density and local fluctuations is central to their results. Correlated and uncorrelated Gaussian samples can share GOE gap statistics while having different global densities. Their Appendix C shows that a deterministic population spectrum can reproduce broad scaling yet miss local sample-covariance spacing behavior. Appendix D exhibits augmentation-dependent changes in scaling while local gap statistics remain comparatively stable. Appendix E separately examines eigenvector localization and alignment; the basis is not determined by the eigenvalue density. Appendix F illustrates actual predictive use through conditional learning-curve calculations, with bulk, sampling and basis assumptions.

Our single-image distance-graph Laplacians, radial coupling graph and transformed damping spectrum are not those dataset-level covariance operators. Although $L = B\,\mathrm{diag}(w)B^T$ has a Gram factorization, incidence columns are constrained, sparse and dependent, weights encode prescribed structure, and $L\mathbf{1} = 0$. A Gram factorization does not establish iid Gaussian sampling, a Wishart law or its asymptotic regime. A bulk-only covariance model also does not automatically cover our full retained positive spectrum and its nonlinear minimum-dependent readout. Neither paper supplies an independently validated quantitative explanation for the present profiles.

8.3 The required density-to-profile prediction

An independently specified smooth log-native density f would, under an additional iid distinct-value approximation, give

$$g(t) = \int f(u)f(u-t)\,du, \qquad q_j = \frac{\int_{I_j\cap B} g(t)\,dt}{\int_B g(t)\,dt}. \tag{16}$$

For uncut positive values with density p and CDF F, equivalently

$$q_j = \int_0^{\infty} p(y)\{F[c_j(1+\epsilon)y] - F[c_j(1-\epsilon)y]\}\,dy. \tag{17}$$

With fixed unfiltered n, the iid expected hit count is $n(n-1)q_j$. For filtered random exposure, Eq. (16) is a population conditional-pair probability or ratio of mean counts, not generally $\mathbb{E}[h_j/N_R]$.

For a constrained finite ensemble the mean one-point density need not determine the pair intensity. If ρ_1 is a counting density and ρ_2 the factorial two-point intensity, exact expected nonself counts integrate ρ_2. Even fixed-n iid values have $\rho_2 = (n-1)\rho_1\rho_1/n$; an uncorrected

product is a Poisson-number or asymptotic factorization. Connected correlations, between-realization density variation and extrema constraints can matter. In particular, Eq. (3) fixes $v_{\min} = \ln 2$ and $u_{\min} = \ln \ln 2$: a model must retain this anchor and its finite pair weights.

Thus global density is a candidate explanation requiring a specified model and quantitative window prediction, while local gap correlations provide complementary information. An observed-spectrum autocorrelation replay is the exact identity in Section 3.2, not evidence that the explanatory model succeeds. Appendix C gives an analytical illustration without fitting or testing it on these data.

9 Interpretation, contribution and remaining tests

The positive empirical contribution is a reproducible comparison of finite structural signatures across stated operators, together with control-specific discrimination and robustness. The recurrence is strongest among the primary hydrogen transformed profile and five image graphs; the embryo and moderate Kerr relationships locate its heterogeneity. The Kerr U/P comparisons establish effects beyond their specified uniform-group and coarse-bin/phase references. Shell-block stability establishes robustness to weight placement changes that retain detailed block multisets. These conclusions remain useful even though the target library does not pass the joint specificity test.

The signatures are functionals of spectral multisets. Isospectral operators have identical signatures; fifteen windows cannot restore information absent from the spectrum. Equation (8) also loses translation/phase information in log coordinates. The method can summarize geometric information carried through a spectrum without identifying a unique geometry or eigenbasis. A common physical carrier, physical-realization law, universal coherence/dissipation sign inversion or unique invariant is not established by these coefficients. The original assumption that preserving a weight histogram necessarily destroys the relevant physical structure is not valid for the present shell multiset reference.

The possible advance beyond existing work is therefore specific. It may be a useful cross-operator application, a compact density-sensitive descriptor complementary to gap statistics, or a way to detect reproducible residuals beyond an independently specified density-and-pair model. Demonstrated general-purpose classification or added value over simple density, quantile, moment and spacing summaries would require a declared task and independent objects. A different observable alone does not establish novelty; a known density mechanism would not automatically remove potential diagnostic usefulness. This two-paper comparison is not an exhaustive priority search.

The smallest useful numerical extension would use the saved hydrogen shell spectra to test a fixed low-complexity density model against retained profile tables, with training-fit uncertainty, a declared endpoint split, the minimum anchor, all fifteen slots and all three widths. Such internal calibration would be exploratory because these endpoints are already seen. Separate adjacent-gap calculations on saved spectra could then test whether local correlations change when the all-pair shape survives, with raw/transformed coordinates, sectors and degeneracy rules fixed first. Neither extension was executed here. A genuinely independent explanatory prediction would derive its density from operator parameters or separate objects and validate on new objects. Broader universality and physical interpretation remain questions for those tests, not revised labels for the failed frozen prediction.

10 Conclusion

The completed finite investigation resolves three questions differently. Structural profile recurrence is strong in several specified cross-domain constructions, but has meaningful exceptions and is not generally exclusive to the original library. Kerr incidence discriminates strongly against two nominated conditional references in both development and angular holdout, while an overtone/Gram-preserving reference is more permissive on holdout. Hydrogen profile shape is robust to shell-block permutation, although aggregate abundance changes with the readout and the short fiber pilot is uninformative. The frozen three-domain library criterion fails at a joint reference fraction of 0.2339.

Together these results support a finite structural signature and a diagnostic method for comparing it. The log-autocorrelation representation identifies what is measured and the mathematical connection an explanatory density model must supply. It does not convert recurrence into a common physical mechanism, nor does related random-matrix theory already explain these particular profiles without that model. A quantitative independent prediction, followed by independent-object and utility tests, is the most direct route to a stronger contribution.

Data and code availability

The accompanying public verification supplement supplies retained numerical inputs, library definitions, compact control information, result tables, executable verification/regeneration code, figure-generation scripts, dependency pins and checksums. Its README distinguishes quick checks of supplied results from full numerical regeneration and records the checks actually performed. It avoids storing the billions of repeated derived matrix cells, which can be reconstructed or recomputed in batches. This publication preparation did not perform a clean full numerical rerun or a new scientific campaign.

Numerical spatial verification starts from the retained centroid inputs. Original photograph redistribution is not asserted: photographic files, thumbnails and overlays are excluded; exact hashes, known acquisition identifiers and the pixel-extraction specification are retained. Six exact acquisition mappings and all seven photographic permission records remain unresolved, so full pixel-level acquisition/replay is not represented as publicly complete. The reserved manuscript identifier is 10.5281/zenodo.23888292; public upload has not occurred during this preparation. The author platform is www.everythingequation.com.

Acknowledgements and author statement

The author developed the research programme and the core manuscript. AI tools were used to support additional numerical work, cross-checking, literature reconciliation, and editorial revision of the existing text. The author retains responsibility for the interpretation and the final manuscript.

A Numerical conventions and verification

The cross-domain execution used Python 3.12.14, NumPy 2.3.5, SciPy 1.17.0 and Pillow 12.2.0. The earlier 4,999-control Kerr execution used NumPy 2.5.4; retained control values distinguish exact input preservation from platform-dependent re-evaluation of a generator. The supplement records versions for its executable subset and plotting workflow. Floating arrays use double precision; retained source hashes bind state, point and library order. Counting is performed on eligible sorted ordered ratios with inclusive window endpoints; no histogram binning or

ratio rounding is introduced. Independent direct-Boolean counters checked selected complete fifteen-slot cases, and a prepared-window acceleration matched every field of four complete 10,000-library reference cases at all widths, including overlap and boundary fixtures.

For spatial eigenvalues the zero rule uses absolute and relative tolerances 10^{-12}: the threshold is the larger of the absolute cutoff and the relative cutoff times maximum eigenvalue magnitude. Hydrogen instead uses $50\epsilon_{\mathrm{mach}} N \max_i |\lambda_i|$ on the full $N = 465$ spectrum. Each requires exactly one eigenvalue within its zero threshold and no negative eigenvalue below the negative threshold; retained positive modes and multiplicities are not deduplicated. Laplacian eigenpair residuals, orthogonality, centroid identities and count comparisons were checked independently. The software suite passed 118 tests; final integrity audits authenticated 413 score datasets, 41,300 batches and 185,850,000 slot counts. The stored observed/conditional representation accounts for 401 full or losslessly reconstructable matrix stores. These audit counts establish execution coverage, not independent sample sizes.

The public quick check is narrower than a clean full rerun: it checks retained numerical tables, definitions, counts, pairings, selected independent numerical reconstructions and the manuscript's claim index as documented in its verification record. Full-regeneration commands are separately specified; source image acquisition is gated as explained above. Platform/BLAS differences may change last-bit eigenvalues, so reproduction uses declared numerical tolerances rather than asserting universal bitwise eigenspectra.

B Invariances and nonidentifiability

For symmetric nonnegative weights,

$$x^T L x = \frac{1}{2} \sum_{i,j} W_{ij}(x_i - x_j)^2 \geq 0. \tag{18}$$

A connected support has the constant vector as its one-dimensional kernel. Multiplying all weights by a common positive factor rescales positive eigenvalues; raw ratios and minimum-normalized log1p ratios remain unchanged. For a numerical protocol with an absolute zero threshold, this statement assumes that the retained positive-mode set is unchanged. Such scale cancellation explains invariance under an overall coupling scale without deriving the coupling constant.

The complete Fejér readout is injective on positive scalar eigenvalues, since

$$f_T'(\lambda) = \frac{(T\lambda + 1)e^{-T\lambda} - 1}{T\lambda^2} < 0. \tag{19}$$

Thus the complete unnormalized readout values determine the original positive eigenvalues for known T. An operator-valued readout determines the operator through the inverse functional calculus under the same spectral hypotheses. Pooled ratios or window profiles do not contain that complete information. For comparison, survival-readout ratios $e^{-T\lambda_i}/e^{-T\lambda_j}$ encode differences and lose a common additive shift. These conditional facts do not establish physical spectral transport between different systems.

The ordered-ratio multiset is unchanged under common positive scaling and under $v_i \mapsto a/v_i$, $a > 0$, the latter interchanging pair orientation. That whole-multiset ambiguity survives any fixed native ratio cutoff even though an asymmetric cutoff breaks reciprocal balance of the conditioned distribution. More general log-autocorrelation ambiguities and coarse windowing further obstruct unique inversion. Label permutation alone leaves both the spectrum and the value-ratio statistic unchanged and is not a nontrivial control for this pooled observable.

C An analytical density illustration, not a fitted explanation

Consider a hypothetical continuous rank model $v(k) = Ak^{-p}$, $p > 0$, with k uniformly distributed on $[k_{\min}, k_{\max}]$. Its log-density, after translation, is a truncated exponential with $a = 1/p$ and $L = p \log(k_{\max}/k_{\min})$. Direct integration of the product density gives

$$g(t) = \frac{a\{e^{-a|t|} - e^{-2aL}e^{a|t|}\}}{2(1 - e^{-aL})^2}, \quad |t| \le L, \qquad g(t) = 0 \text{ otherwise.} \tag{20}$$

For example, at $t \ge 0$ the integral is proportional to $e^{-at}\int_0^{L-t} e^{-2au}\,du$, yielding the expression above; symmetry supplies negative t. With L fixed, $a \to 0$ gives $(L - |t|)/L^2$. The parameters p and L are not independent when rank bounds are fixed. Integrating this density over Eq. (9), with the actual cutoff, supplies explicit window predictions once the model is independently specified. This calculation illustrates a possible bridge from a broad rank law such as that studied by Levi and Oz [2]; it was not fitted to, or numerically validated against, the present spectra. Substituting an exact observed spectrum would instead return the identity in Eq. (8).

D Complete core comparisons and native summaries

Table 6 retains all 28 unique primary-core pairs at each tolerance, with both coefficient types and paired-bank positions. The full 17-view table, symmetric entries, statuses, all control-profile summaries and sensitivity results are supplied electronically. Table 7 gives the native target incidence and bank midposition of all observed views. Primary spatial abundance is 1% UNION even where profile comparisons use 3%.

Table 6: All primary-core pairs: target coefficients and conservative paired-G fractions. Spearman is primary descriptive; Pearson is secondary.

Left	Right	ϵ	ρ_s	$F_{G,s}$	r_P	$F_{G,P}$
Kerr	H30 log $1p$	3%	0.52143	0.60200	0.38983	0.50530
Kerr	Embryo	3%	0.66848	0.00860	0.54929	0.01900
Kerr	Galaxy	3%	0.65708	0.31630	0.34932	0.62020
Kerr	Pollen	3%	0.38277	0.54830	0.43262	0.40290
Kerr	Leaf	3%	0.52189	0.61290	0.40281	0.45970
Kerr	Shroud	3%	0.38399	0.60770	0.38992	0.45810
Kerr	Snowflake	3%	0.53335	0.64320	0.35456	0.55530
H30 log $1p$	Embryo	3%	0.23900	0.54060	-0.25984	0.85300
H30 log $1p$	Galaxy	3%	0.92063	0.97900	0.98928	0.49600
H30 log $1p$	Pollen	3%	0.88641	0.86000	0.95464	0.61710
H30 log $1p$	Leaf	3%	0.99553	0.16900	0.98673	0.69500
H30 log $1p$	Shroud	3%	0.94868	0.71350	0.97981	0.46000
H30 log $1p$	Snowflake	3%	0.98743	0.44180	0.99637	0.10530
Embryo	Galaxy	3%	0.26522	0.31930	-0.30299	0.82760
Embryo	Pollen	3%	-0.13177	0.55510	-0.23573	0.82000
Embryo	Leaf	3%	0.22123	0.56050	-0.25919	0.81670
Embryo	Shroud	3%	0.01326	0.63510	-0.26397	0.82550
Embryo	Snowflake	3%	0.22484	0.57220	-0.30057	0.83800
Galaxy	Pollen	3%	0.89402	0.70270	0.91855	0.67060
Galaxy	Leaf	3%	0.92145	0.85170	0.96477	0.81530
Galaxy	Shroud	3%	0.85055	0.93580	0.95719	0.64790
Galaxy	Snowflake	3%	0.92896	0.98590	0.99235	0.33340
Pollen	Leaf	3%	0.88720	0.77980	0.98754	0.24830
Pollen	Shroud	3%	0.93435	0.72360	0.98982	0.31790
Pollen	Snowflake	3%	0.89443	0.63730	0.95739	0.78900
Leaf	Shroud	3%	0.94953	0.69710	0.99863	0.04760
Leaf	Snowflake	3%	0.98831	0.29460	0.98911	0.95950
Shroud	Snowflake	3%	0.95727	0.23330	0.98489	0.78600
Kerr	H30 log $1p$	1%	0.43571	0.81390	0.34661	0.47240

Table 6: All primary-core pairs (continued). Spearman is primary descriptive; Pearson is secondary.

Left	Right	ϵ	ρ_s	$F_{G,s}$	r_P	$F_{G,P}$
Kerr	Embryo	1%	0.62299	0.09380	0.62517	0.04940
Kerr	Galaxy	1%	0.54927	0.64320	0.31747	0.56500
Kerr	Pollen	1%	0.24175	0.82110	0.41242	0.32030
Kerr	Leaf	1%	0.43828	0.81640	0.37102	0.41220
Kerr	Shroud	1%	0.27482	0.78150	0.35665	0.41810
Kerr	Snowflake	1%	0.45796	0.77810	0.31555	0.50690
H30 $\log 1p$	Embryo	1%	0.26856	0.39160	-0.18999	0.65770
H30 $\log 1p$	Galaxy	1%	0.92328	0.87620	0.98887	0.32180
H30 $\log 1p$	Pollen	1%	0.88641	0.77540	0.95350	0.63680
H30 $\log 1p$	Leaf	1%	0.99463	0.28980	0.98493	0.77460
H30 $\log 1p$	Shroud	1%	0.94492	0.64310	0.97916	0.42810
H30 $\log 1p$	Snowflake	1%	0.98652	0.51560	0.99645	0.07060
Embryo	Galaxy	1%	0.31795	0.22260	-0.19019	0.53490
Embryo	Pollen	1%	-0.07420	0.35640	-0.17174	0.61250
Embryo	Leaf	1%	0.26904	0.37480	-0.18236	0.59490
Embryo	Shroud	1%	0.06933	0.45930	-0.18215	0.58350
Embryo	Snowflake	1%	0.28890	0.37400	-0.20790	0.58520
Galaxy	Pollen	1%	0.89484	0.23500	0.92326	0.39380
Galaxy	Leaf	1%	0.92493	0.62390	0.96373	0.62700
Galaxy	Shroud	1%	0.85324	0.84130	0.95848	0.43300
Galaxy	Snowflake	1%	0.94139	0.83010	0.99261	0.22110
Pollen	Leaf	1%	0.88799	0.25230	0.98970	0.17290
Pollen	Shroud	1%	0.93011	0.96500	0.99050	0.29080
Pollen	Snowflake	1%	0.89648	0.00960	0.95751	0.70830
Leaf	Shroud	1%	0.94661	0.69210	0.99860	0.03340
Leaf	Snowflake	1%	0.98828	0.09740	0.98733	0.97290
Shroud	Snowflake	1%	0.95974	0.00370	0.98448	0.69800
Kerr	H30 $\log 1p$	0.5%	0.41644	0.74510	0.39744	0.33290
Kerr	Embryo	0.5%	0.34075	0.54540	0.42209	0.29020
Kerr	Galaxy	0.5%	0.48599	0.75700	0.38599	0.37830
Kerr	Pollen	0.5%	0.28204	0.64100	0.47416	0.19790
Kerr	Leaf	0.5%	0.40645	0.79230	0.43228	0.26110
Kerr	Shroud	0.5%	0.25976	0.75470	0.41679	0.26570
Kerr	Snowflake	0.5%	0.41300	0.80120	0.36863	0.36280
H30 $\log 1p$	Embryo	0.5%	0.04482	0.81960	-0.28975	0.87260
H30 $\log 1p$	Galaxy	0.5%	0.96373	0.16670	0.99273	0.05980
H30 $\log 1p$	Pollen	0.5%	0.88518	0.93970	0.95481	0.51960
H30 $\log 1p$	Leaf	0.5%	0.99642	0.07010	0.98330	0.82800
H30 $\log 1p$	Shroud	0.5%	0.94765	0.55880	0.97940	0.39140
H30 $\log 1p$	Snowflake	0.5%	0.98921	0.24550	0.99552	0.20500
Embryo	Galaxy	0.5%	0.05359	0.76390	-0.27392	0.76320
Embryo	Pollen	0.5%	-0.28557	0.79360	-0.27104	0.84700
Embryo	Leaf	0.5%	0.04490	0.79960	-0.28458	0.82850
Embryo	Shroud	0.5%	-0.15599	0.85300	-0.27543	0.80080
Embryo	Snowflake	0.5%	0.04523	0.81330	-0.30535	0.82210
Galaxy	Pollen	0.5%	0.90145	0.02900	0.95245	0.02970
Galaxy	Leaf	0.5%	0.96546	0.06620	0.97699	0.18390
Galaxy	Shroud	0.5%	0.89408	0.43940	0.97801	0.08500
Galaxy	Snowflake	0.5%	0.97247	0.32650	0.99579	0.02540
Pollen	Leaf	0.5%	0.88879	0.03490	0.99074	0.13160
Pollen	Shroud	0.5%	0.93435	0.92280	0.99040	0.29580
Pollen	Snowflake	0.5%	0.89117	0.75990	0.95625	0.74100
Leaf	Shroud	0.5%	0.95123	0.02430	0.99855	0.03290
Leaf	Snowflake	0.5%	0.98918	0.04960	0.98396	0.99540
Shroud	Snowflake	0.5%	0.95434	0.32170	0.98285	0.76280

Table 7: All observed native target views. Midposition is relative to the same target plus 9,999 G population; raw hydrogen, bright images and adult portrait remain secondary.

View	N_R	Window	Count	Incidence	Midposition
Kerr	272049	3%	SUM	0.30581	0.95435
H30 $\log 1p$	214832	3%	UNION	0.10190	0.44780
H30 raw	214832	3%	UNION	0.12159	0.07820
embryo	870	1%	UNION	0.05517	0.43155
embryo bright	1190	1%	UNION	0.05042	0.95330
galaxy	11990	1%	UNION	0.04370	0.55115
galaxy bright	93330	1%	UNION	0.02674	0.50220
pollen	997002	1%	UNION	0.02529	0.35660
pollen bright	1282556	1%	UNION	0.03149	0.51300
adult human	2652	1%	UNION	0.01357	0.17185
adult human bright	4830	1%	UNION	0.05404	0.58295
leaf	325470	1%	UNION	0.04696	0.60690
leaf bright	145542	1%	UNION	0.02020	0.35485
shroud	153272	1%	UNION	0.03982	0.69565
shroud bright	81510	1%	UNION	0.04368	0.83610
snowflake	493506	1%	UNION	0.03931	0.64350
snowflake bright	396270	1%	UNION	0.04596	0.52875

E Material reconstruction corrections

Table 8: Reconstructed H30 counts with 214,832 eligible ordered nonself ratios. These replace unreproduced manuscript totals.

	3%		1%		0.5%	
Readout	SUM	UNION	SUM	UNION	SUM	UNION
Raw	27,853	26,122	9,186	9,186	4,563	4,563
log1p	23,495	21,892	7,800	7,800	3,895	3,895

The 465-state graph gives the raw and transformed counts in Table 8; 464 positive modes imply $464 \times 463 = 214,832$ ordered nonself pairs. Earlier reported totals 28,941/31,204 and denominator 214,576 are not reproduced under the stated minimum-normalized relative-window construction. The earlier printed fifteen marginals also sum to 30,264, below a purported 31,204 UNION, contrary to Eq. (7). These numbers are not retained as established results. Minimum-versus-median normalization and log-distance-versus-relative windows explain some other archived count differences, but do not identify the lost 31,204 run. A common eigenvalue scale alone cannot change raw or own-minimum-normalized ratios.

Null-stage choices also matter. Retained raw-uniform controls gave raw UNION standardized difference about -13.286; drawing raw uniform values and then applying the primary transform gave about $+0.456$, whereas uniform sampling in the transformed range gave about -21.562. They are different reference laws, not interchangeable calibrations. The unsupported historical H30 +7.7 claim is not used. The present shell-reference findings answer a separate preservation question.

H12 is a distinct 78-state construction: it omits same-n links and uses absolute radial amplitudes with an $m = 0$ angular factor rather than squared radial weights. Its 506 edges, 77 positive modes, filtered exposures and counts must not substitute for H30. Successful deterministic H12 count checks remain valid in that construction; missing original random streams and phase conventions prevent transferring its stochastic or synthetic-generator claims to this paper. Likewise, unrecovered historical image feature maps, the sphere/speckle inputs and separate

direct-distance protocols are not represented as results of the present spectral reconstruction. No universal physical/nonphysical boundary or synthetic-impossibility claim follows.

For Kerr, the electromagnetic local Fejér row has archived standardized effect 12.2713 and width 2.3290. The gravitational local row has a different archived calibration (11.3464, width 2.5887); a retained 100-draw plug-in uniform-Fejér bank at the same gravitational point yields 10.6137. These reference realizations are distinct. The original random stream of the local scan rows is unavailable, so their deterministic source values are not advertised as newly reproduced tail calibrations. The grouped-endpoint 4,999-draw U reference and the R/P experiments in the main text supply the current explicit conditional comparisons.

References

[1] Y. Y. Atas, E. Bogomolny, O. Giraud, and G. Roux. Distribution of the ratio of consecutive level spacings in random matrix ensembles. *Physical Review Letters*, 110:084101, 2013. 10.1103/PhysRevLett.110.084101.

[2] Noam Itzhak Levi and Yaron Oz. The underlying universal statistical structure of natural datasets. In *Proceedings of the 42nd International Conference on Machine Learning*, volume 267 of *Proceedings of Machine Learning Research*, pages 34020–34043. PMLR, 2025. URL https://proceedings.mlr.press/v267/levi25c.html.

[3] Emanuele Berti, Vitor Cardoso, and Andrei O. Starinets. Quasinormal modes of black holes and black branes. *Classical and Quantum Gravity*, 26(16):163001, 2009. 10.1088/0264-9381/26/16/163001.

[4] Leo C. Stein. qnm: A Python package for calculating Kerr quasinormal modes, separation constants, and spherical-spheroidal mixing coefficients. *Journal of Open Source Software*, 4 (42):1683, 2019. 10.21105/joss.01683.

[5] Fan R. K. Chung. *Spectral Graph Theory*, volume 92 of *CBMS Regional Conference Series in Mathematics*. American Mathematical Society, Providence, RI, 1997. 10.1090/cbms/092.